VIII Modeling Rayleigh-Taylor Instability of a Sedimenting Suspension of Several Thousand Circular Particles in Direct Numerical Simulation

In this chapter we study the sedimentation of several thousand circular particles in 2D using the method of distributed Lagrange multipliers for solid-liquid flow. The simulation gives rise to fingering which resembles Rayleigh-Taylor instabilities. The waves have a well defined wavelength and growth rate which can be modeled as a conventional Rayleigh-Taylor instability of heavy fluid above light. The heavy fluid is modeled as a composite solid–liquid fluid with an effective composite density and viscosity. Surface tension cannot enter this problem and the characteristic short wave instability is regularized by the viscosity of the solid liquid dispersion. The dynamics of the Rayleigh-Taylor instability are studied using viscous potential flow generalizing work of Joseph, Belanger, and Beavers 1999 to a rectangular domain bounded by solid walls; an exact solution is obtained.

The data in this chapter is generated by the direct numerical simulation of solid–liquid flow using a distributed Lagrange multiplier/fictitious domain method (see Glowinski, Pan, Hesla & Joseph 1999, Glowinski, Pan, Hesla, Joseph & Periaux 2000). The calculation is carried on fixed triangular mesh on which fluid equations are satisfied everywhere. Rigid motions of the portions of the fluid occupied by solids are accomplished by a strategic choice of a Lagrange multiplier field there. The method has a certain elegance in that the rigid motion constraint on the fluid is associated with a multiplier field in a manner analogous to the way in which the pressure in an incompressible flow is a multiplier field associated with the constraint on incompressibility. The details of the computation have been given in the cited references and will not be repeated here.

Simulation Data

The specific simulations discussed in this chapter concern the *sedimentation* of several thousand disks settling down in a 2D rectangular box filled with water of density $\rho_1 = 1$ g/cm^3 and viscosity $\nu_1 = 0.01$ poise. The disks of same diameter are initially arranged like those shown in Figure VIII.2(a), Figure VIII.3(a) and Figure VIII.4(a). We also have shown in Figure VIII.1 the relative position of disks in three different lattices mentioned above and call them square, hexagonal, and rectangular respectively. In a square lattice the gap sizes in the horizontal and vertical directions are the same. Similarly in a hexagonal case the gap size in the horizontal direction and the one between rows in the vertical direction are the same. But in the rectangular case the gap size in the horizontal direction is 1.2642 times of the one in the vertical direction.

The diameters of disks are $8/192$ cm, $10/192$ cm, $11/192$ cm, $12/192$ cm, $13/192$ cm, $14/192$ cm, $15/192$ cm, and $16/192$ cm. The density of disks is $\rho_p = 1.1$ g/cm^3. The volume fraction of disks in the initial lattice is the ratio of the area A_p of the disks to the total area A_T of the initial lattice

$$\phi = \frac{A_p}{A_T} = \frac{N\pi d^2/4}{HW} \tag{VIII.1}$$

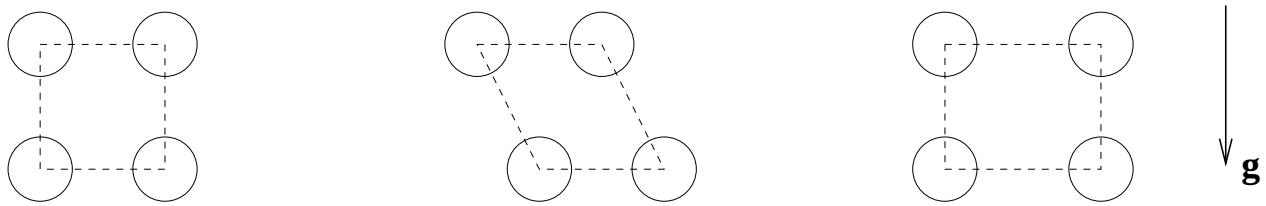

Figure VIII.1: *Initial lattices.*

where N is the total number of the disks, d is the diameter of the disks, H is the height of the initial lattice, and W is the width of the box. In the simulation we have chosen 4, 6, 8, 10, and 12 cm as the width W and the height of the box is always 12 cm.

In the cases where the initial lattice is square, there are 60 rows of disks in most of the cases. In each row, there are 42, 63, 84, 105, and 126 disks as the width is 4, 6, 8, 10, and 12 cm, respectively. To test whether more rows of disks can have different effect, we also tested 80 rows cases in a 2D box of width 10 cm and height 12 cm with diameters varying from 10/192 cm to 16/192 cm.

In hexagonal cases there are 6270 disks staggered at the top of the box (see Figure VIII.3(a)). There are 60 rows and in each row there are either 104 or 105 disks. The width and the height of the box are 10 cm and 12 cm respectively. The diameter of disks varies from 10/192 cm to 16/192 cm. In Figure VIII.3(b), the snapshot of the sedimentation of 6270 disks of diameter 10/192 cm in a 2D box is shown.

In rectangular cases, there are 80 columns at the top of the box. We tested two sets of cases in which the number of rows is either 60 of 80 in order to probe the effect of the number of rows. The diameter of disks varies from 10/192 cm to 16/192 cm. In Figure VIII.4, there are snapshots of the sedimentation of 4800 and 6400 disks of diameter either 10/192 cm or 16/192 cm in a 2D box.

In all simulations the averaged particle Reynolds number at each time step is less than 3. The maximal individual particle Reynolds number among all simulations is about 11. In each case, simulation gives rise to fingering which resembles Rayleigh-Taylor instabilities (Figures VIII.2, VIII.3, and VIII.4). The waves have a well defined wavelength and growth rate which we shall model as a conventional Rayleigh-Taylor instability of heavy fluid above light. The arrangement of sedimenting particles is asymmetric, flat on the top (most of portion on the top in the hexagonal case) and corrugated at the bottom. The drag on a single disk is smaller than when it is among many so that isolated disks on the bottom fall out of the lattice and isolated disks on the top fall into the lattice.

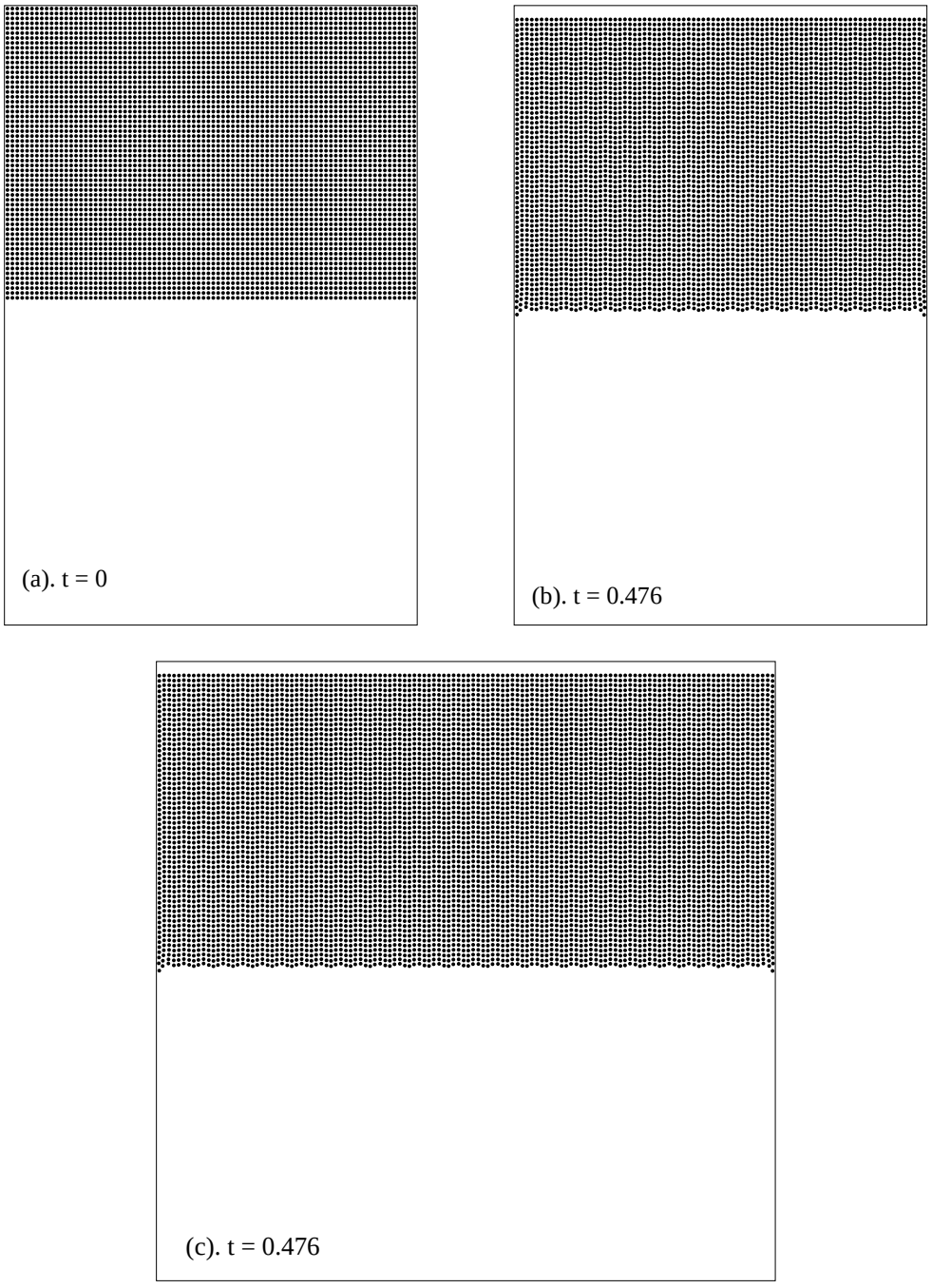

Figure VIII.2: *Snapshots of the sedimentation of 5040 (top, $W = 8$ cm) and 7560 (bottom, $W = 12$ cm) disks of diameter 14/192 cm in 2D. The initial lattice is square.*

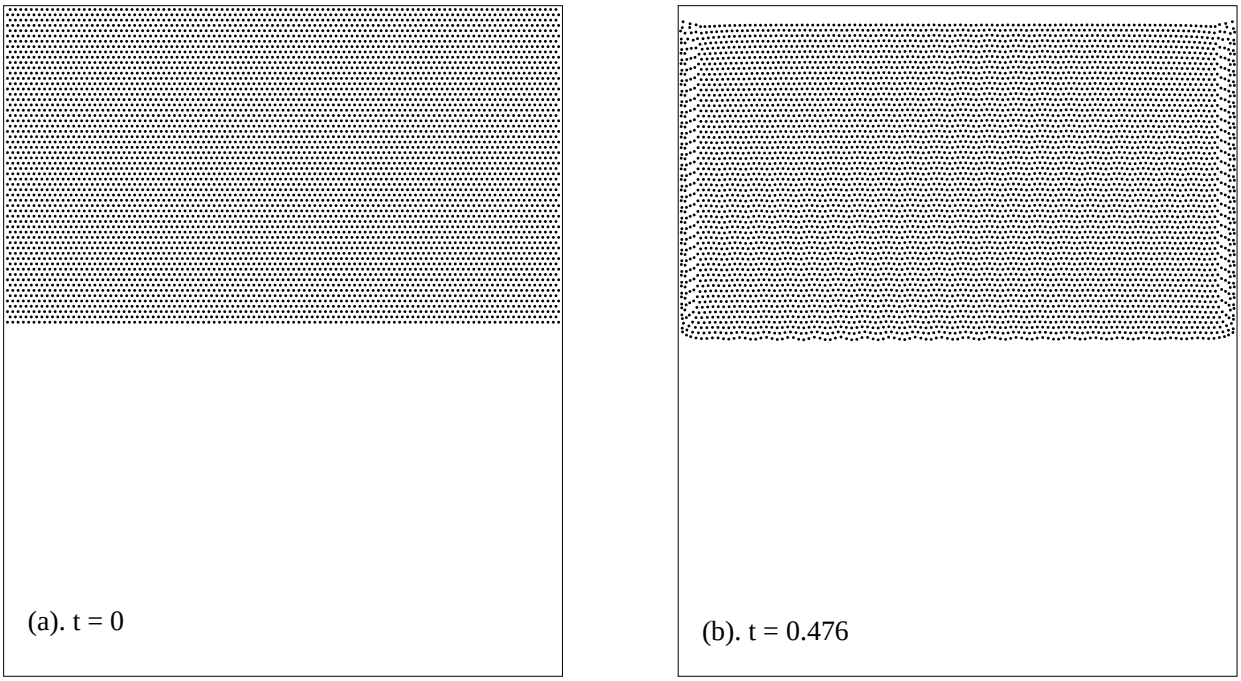

Figure VIII.3: *Snapshots of the sedimentation of 6270 disks of diameter 10/192 cm in 2D ($W = 10$ cm). The initial lattice is hexagonal.*

Two-fluid Model

We turn next to the two-fluid modeling of the instability of the sedimenting suspension just described. The basic idea is to regard the particle laden portion of the sedimenting suspension (shown in Figures VIII.2, VIII.3, and VIII.4) as an effective fluid with an effective viscosity η_2 and an effective density $\rho_2 = (1-\phi)\rho_1+\phi\rho_p$ and, of course, zero surface tension γ; then we have two fluids, an effective one above and water below. The dynamics of this two-fluid problem can be analyzed using viscous potential flow (Joseph and Liao 1994). Joseph, Belanger and Beavers 1999 showed that the wavelengths and the growth rates obtained with viscous potential flow differ from those obtained from a fully viscous analysis by only a few percent. The success of the potential flow analysis arises from the fact that main action of viscosity is in the viscous part of the normal stress acting here in our problem through the effective viscosity of the solid–liquid suspension. Surface tension can not enter into this problem so that the effective viscosity is the only mechanism which regularizes an otherwise ill–posed problem in which the growth rate increases like $1/\sqrt{\lambda}$, tending to infinity with ever shorter waves (Joseph and Saut 1990).

The analysis of Rayleigh-Taylor instability using viscous potential flow can be carried out in an infinitely extended domain using the method of normal modes with disturbance proportional to

$$e^{nt}e^{i(k_x x+k_y y)}e^{\pm qz} \tag{VIII.2}$$

where, for viscous potential flow

$$q = k = \sqrt{k_x^2 + k_y^2} \tag{VIII.3}$$

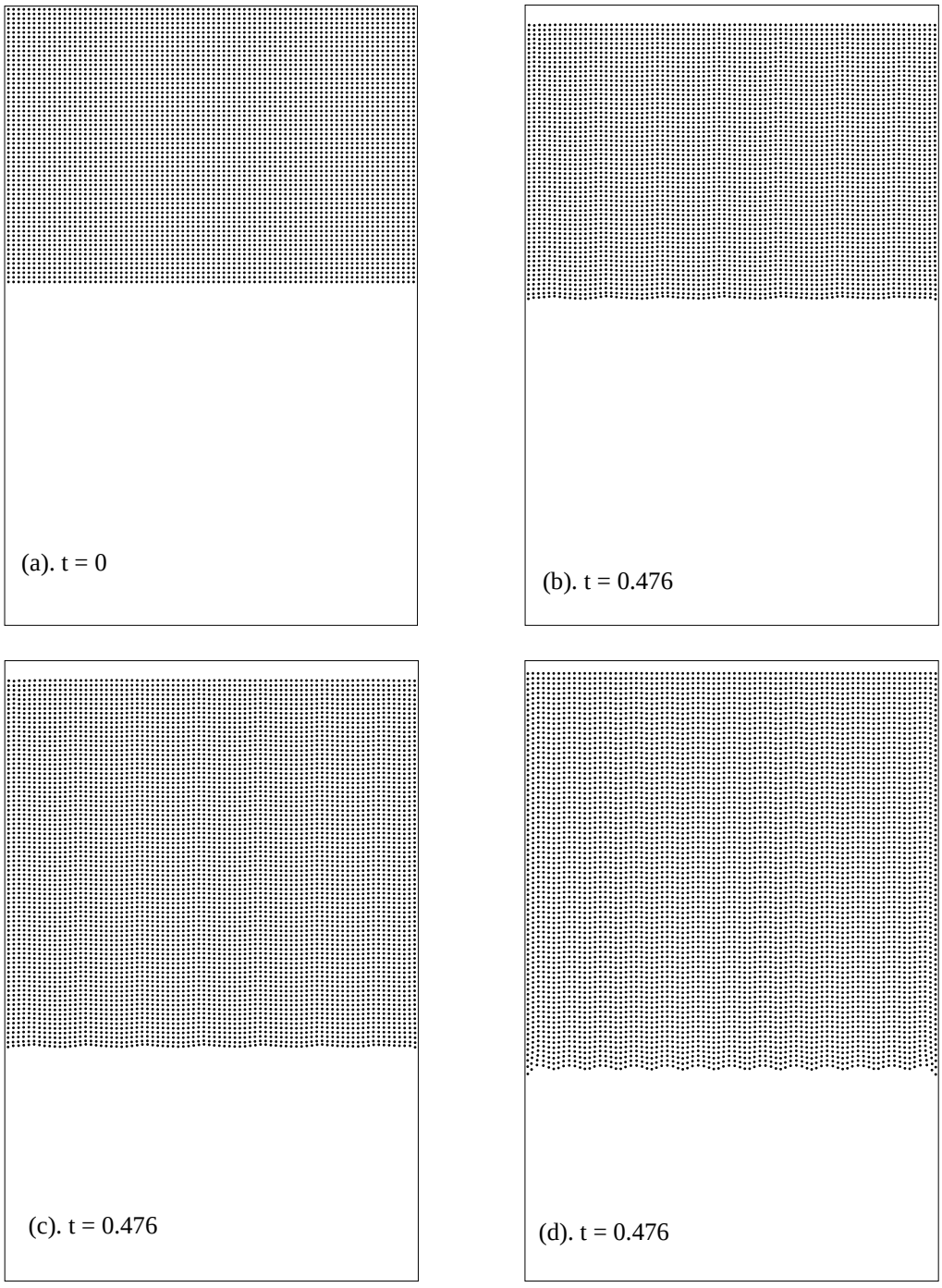

Figure VIII.4: *Snapshots of the sedimentation of 4800 (top) and 6400 (bottom) disks in 2D ($W = 8$ cm). The diameter of disks in (a), (b) and (c) is 10/192 cm and the diameter of disks in (d) is 16/192 cm. The initial lattice is rectangular.*

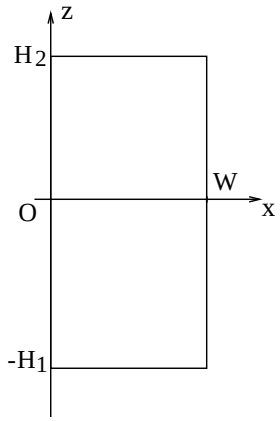

Figure VIII.5: *Initial configuration.*

where the z increases against gravity $g = 980.6635$ cm/sec and the sign $\pm k$ chosen so that the amplitude decays at infinity. The analysis leads to the following dispersion relation (equation (25) of Joseph, Belanger and Beavers 1999)

$$\rho_2 + \rho_1 = \frac{k}{n^2}(\rho_2 - \rho_1)g - \frac{\gamma k^3}{n^2} - \frac{2k^2}{n}(\eta_2 + \eta_1). \tag{VIII.4}$$

Equation (VIII.4) depends on k_x and k_y only through k in (VIII.3); hence (VIII.4) is valid in both two and three dimensions and it applies to the planar problem under discussion.

To get k which maximizes n (with zero surface tension, $\gamma = 0$), we differentiate (VIII.4) with respect to k, set $dn/dk = 0$ and find that

$$k = \frac{(\rho_2 - \rho_1)g}{4n(\eta_2 + \eta_1)}. \tag{VIII.5}$$

Substituting (VIII.5) into (VIII.4), we get the growth rate

$$n^3 = \frac{(\rho_2 - \rho_1)^2 g^2}{8(\eta_2 + \eta_1)(\rho_2 + \rho_1)}, \tag{VIII.6}$$

and the associated wave length is given by

$$k^3 = \frac{(\rho_2^2 - \rho_1^2)g}{8(\eta_2 + \eta_1)^2}. \tag{VIII.7}$$

We also carry out similar analysis in the rectangular domain of the computation as shown in Figure VIII.5, in which we can construct the viscous potential flow. Let W be the width of the domain, H_2 is the height of the fluid-solid mixture above water of height H_1. Then the velocity obtained from a potential ψ is $\mathbf{u} = \nabla\psi$. Let $z = \zeta(x,t)$ be the interface. The normal stress balance applied on $z = 0$ may be reduced, using Bernoulli's equation, to

$$-\gamma\frac{\partial^2\zeta}{\partial x^2} = \left[|\rho\frac{\partial\psi}{\partial t}|\right] + [|\rho|]\, g\zeta + 2\left[|\rho\frac{\partial^2\psi}{\partial z^2}|\right] \tag{VIII.8}$$

The kinetic equation of motion of the perturbated free surface $\omega = \partial\zeta/\partial t$ implies that

$$\frac{\partial\zeta}{\partial t} = \frac{\partial\psi_1}{\partial z} = \frac{\partial\psi_2}{\partial z} \tag{VIII.9}$$

The normal derivative of the potential $\psi(x, z, t)$ must vanish on the solid wall, $\partial\psi/\partial x = 0$ on $x = 0$ and $x = W$, $\partial\psi_1/\partial z = 0$ on $z = -H_1(< 0)$, and $\partial\psi_2/\partial z = 0$ on $z = H_2(> 0)$. The normal mode solutions corresponding to (VIII.8) on the bounded domain are

$$\begin{cases} \psi_1 = A_1 e^{nt} \cos kx \cosh k(z + H_1), \text{ for } z < 0, \\ \psi_2 = A_2 e^{nt} \cos kx \cosh k(z - H_2), \text{ for } z > 0, \\ \zeta = A_3 e^{nt} \cos kx \end{cases} \tag{VIII.10}$$

where

$$k = (m + 1)\pi/W. \tag{VIII.11}$$

It is convenient to treat k as a continuous variable.

After inserting (VIII.10) into (VIII.8) and (VIII.9) we find the dispersion relation

$$(\rho_2 - \rho_1)gk - \gamma k^3 = n^2 \left(\frac{\rho_1}{\tanh kH_1} + \frac{\rho_2}{\tanh kH_2} \right) + 2nk^2 \left(\frac{\eta_1}{\tanh kH_1} + \frac{\eta_2}{\tanh kH_2} \right). \tag{VIII.12}$$

The analysis of (VIII.12) proceeds along conventional lines, we find the k which maximizes n; this k is such that kH_1 and kH_2 is never smaller than 29 in those simulation cases and two $\tanh$'s in (VIII.12) are almost one giving rise to (VIII.4). The comparison of computation and the model may then proceed on the basis of (VIII.4).

Comparison of Two-fluid Model and Simulation

The "effective" viscosity η_2 of the solid-liquid dispersion is unknown and may be defined by our stability analysis using the following procedure. We first select the associated wavelength $k_0 = 2\pi/\lambda$ where λ is the wavelength determined by the numerical experiment. From (VIII.7) we can obtain the value of the effective viscosity η_2 and then the associated growth rate by (VIII.6). The determination of a growth rate from numerical simulation is carried out by fitting the growth in the wave amplitude to be^{nt}. The wave amplitude is the distance of the wave crest defined by a line through the centers of disks in the bottom row. The time step is 0.001 sec and the firest record of distortion of the line of centers through the bottom row of disks is $t = 0.026$. Values of the amplitude used in the curve fitting are at 0.025 second intervals from $t = 0.026$ to $t = 0.476$. In Figure VIII.6, a set of amplitudes and the curve are shown for the case in Figure VIII.4(c).

The aforementioned procedure for determining the effective viscosity of sedimenting disks from a stability calculation has been implemented for a large number of cases and the results obtained are presented in Tables 1 through 12 and Figures VIII.9 through VIII.11. The data has

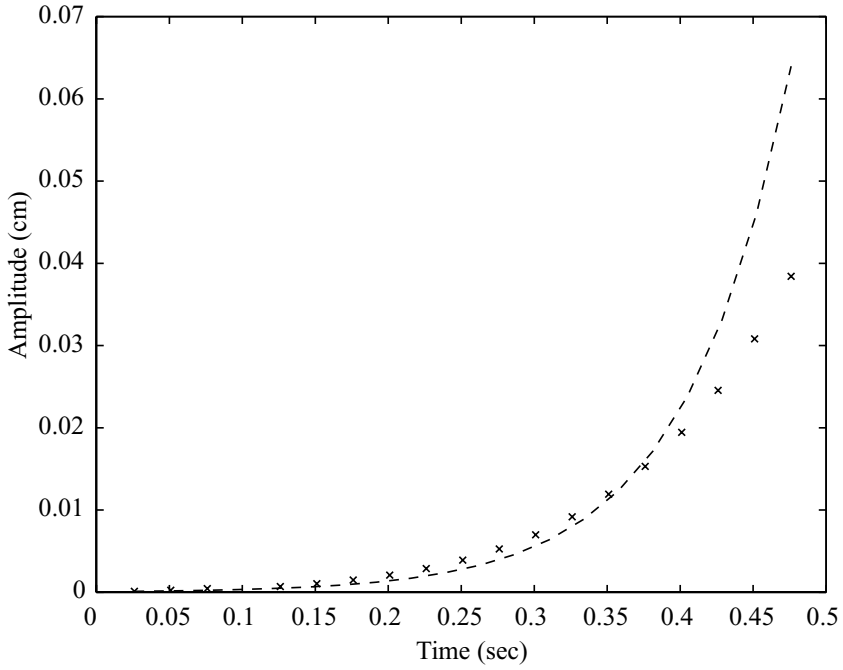

Figure VIII.6: *Amplitude vs. time for the simulation of instability of 6400 disks shown in Figure VIII.4(c). The dashed line is obtained by curve fitting.*

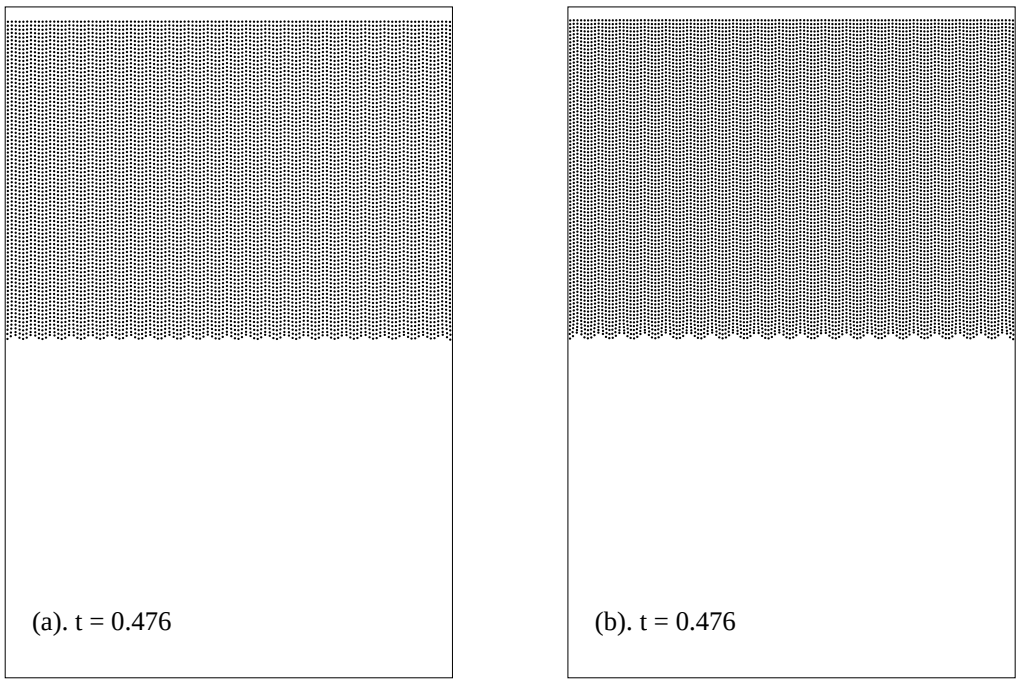

Figure VIII.7: *Snapshots of the sedimentation of 9628 disks (left) and 11340 disks (right) of diameter 8/192 cm in 2D ($W = 8$ cm). The initial lattice is square.*

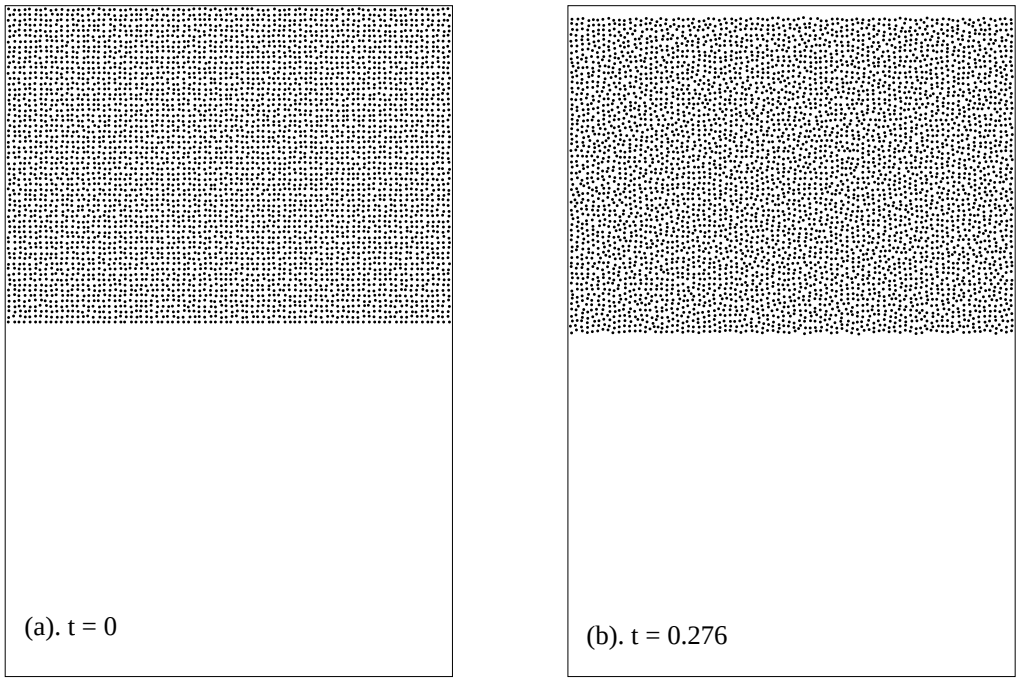

Figure VIII.8: *Snapshots of the sedimentation of 5040 disks of diameter 10/192 cm in 2D ($W = 8$ cm). The initial lattice is disordered.*

been sorted by the geometry of the initial lattice of particles; square, hexagonal or rectangular (Figure VIII.1). In each of these three categories we vary the width and height of the initial lattice by adding or subtracting rows and columns of disks. Each table was indexed by the volume fraction of disks; different volume fractions were created basically by changing the size of the particles.

The procedure we have adopted requires that we assess the success of the modeling by comparing the growth $n(K_0, \eta_2)$ with growth rate from simulation. The largest discrepancy (Table VIII.1) is of the order 30% but the error is less than 10% in the most of cases. In general the errors are greater for small volume fractions and the largest errors occur at small volume fraction in the narrowest ($W = 4$ cm in Table VIII.1).

The data for the square lattice in Table VIII.1 through 6 can be compared with the hexagonal lattice in Table VIII.7 and in the rectangular lattice in Tables 8 through 10. The initial lattice of disks is not modeled and it must have an effect. Obviously if most of the disks were in a ball, it would be necessary at least to prescribe the distribution of volume fraction at the initial instant. Results shown in Table VIII.4 (square) and Table VIII.7 (hexagonal) under otherwise identical conditions do not reveal any important differences; the columns giving the effective viscosity for these two cases match closely and can be seen graphically in Figure VIII.10. However, an examination of the details of the instability in the region near the wall shows a dramatic difference between the square (Figure VIII.2), the hexagonal (Figure VIII.3) and the rectangular (Figure VIII.4). The staggered disks in the hexagonal case are such that only every other row of disks is near the wall, so the wall region has a lower solid fraction and is "weaker" there in such a way the whole bed sinks even as Rayleigh-Taylor waves develop. It is clear that the major effects of the wall are confined

to a wall layer.

When adding more rows to some existing cases, the results shown in Tables 4 and 6 (square) and Tables 8 and 9 (rectangular) again do not reveal any important differences; the columns giving the effective viscosity for these two cases match closely as can be seen graphically in Figures VIII.9 and VIII.11.

Since rectangular lattices are clearly more anisotropic than square ones, much greater differences in the effective viscosity when calculated at the same volume fraction in simulations starting from square and rectangular lattices of disks are evident in comparisons of Tables 3 and 8 and summarized in Figure VIII.11.

To test whether different size particles with same volume fraction would give rise to the same result, we used smaller disks of diameter 8/192 cm in simulations with square lattice. The results are shown in Figure VIII.7 and Table VIII.11. Comparing the results in Table VIII.3 with same dimension and about the same volume fraction and H_2, again we found that the effective viscosity is not uniquely determined by the volume fraction.

We also considered a disordered initial lattice which was generated from a square lattice by moving disks in the horizontal and vertical directions randomly within a given distance except those disks in the bottom row which were only allowed to move in the horizontal direction. This initial configuration is not really a random one. (To generate a random initial configuration with a sharp and flat interface, we have to have many much smaller particles. This is beyond the capability of our code for now.) The results are shown in Figure VIII.8 and Table VIII.12. We still can find the development of waves in Figure VIII.8. We believe that the distribution of disks in these rows right above the bottom row is a perturbation which has strong influence to the development of the interface. The viscosity is consistent with those of square and hexagonal cases with wider width (greater than or equal to 8 cm) and about the same solid volume fraction.

Discussion and Conclusions

The direct 2D simulation of the sedimentation of a close packed array of circular particles into a rectangular box filled with water gives rise to fingers of particles with a wave structure which resembles that which arise from Rayleigh-Taylor instability of heavy fluid above light. The wave length and growth rate of falling particles can be compared with a two-fluid model of the Rayleigh-Taylor instability using viscous potential flow. The particle-fluid mixture is modeled as a heavier than water fluid with an effective density and viscosity. The effective density function of the solid fraction is given by the formula $\rho(\phi) = \rho_p\phi + \rho_f(1-\phi)$ which can be justified by ensemble and other kinds of averaging. Interfacial tension can not enter at the nominal water-mixture interface. The two-fluid model used here to study the Rayleigh-Taylor instability then is fixed when the hindered settling function $f(\phi)$, which determines the effective viscosity $\eta(\phi) = \eta_w f(\phi)$ where η_w is the viscosity of water, is known. Many formulas have been proposed (see, for example, Figure 3 in Poletto & Joseph 1995) and none are perfect.

The effective viscosity of a suspension is a way of describing the flow resistance due to internal friction in a slurry. The resistance can depend on factors like wall proximity, particle size, particle

distribution and other factors even when the solid fraction is fixed. Clumped particles fall faster than well mixed particles, particles near walls fall more slowly. The flow type is also a factor, the effective viscosities of settling, shear and extensional flows are in general different even when the volume fraction is fixed. It is necessary to think of an effective viscosity of a dispersion under well specified conditions; one suit will not fit all.

In our study we focus our attention on the effective viscosity functions of the volume fraction which gives rise to arrangements between computational experiments and two-fluid theory in a restricted situation; we choose the viscosity function to obtain the same number of waves from theory and numerical experiments. The theory may then be used to predict the growth rate and this theoretical value can be checked against numerical experiments. Theoretical and experimental values are listed in last two columns of Tables 1–12 and the agreements are satisfactory.

We have already argued that effective property models live only in well prescribed situations. This is a negative for modeling because besides the model we must specify the situations in which such model exists. In this chapter we determined viscosity function

$$\eta(\phi; W, H_1, H_2, d, I)$$

where different functions of ϕ are obtained when the bed geometry W, H_1 and H_2 (Figure VIII.5), the particle size d and the initial lattice I (Figure VIII.1) are varied.

The asymptotic case of a semi-infinite bed in which W, H_1 and H_2 tend to infinity is of specific interest since in this case there is no length to compare with the circle diameter d; the instability must be independent of d but could depend on the initial lattice I of particles. This asymptotic case might be the most universal, the one closest to our two-fluid model on the semi-infinite domain leading to (VIII.4).

The periodic box of length W used in our exact solution (VIII.10) can be repeatedly extended onto the infinity, but the ratio d/W then is a solution parameter. The asymptotic limit of a semi-infinite domain mentioned above would be achieved when

$$d/W \to 0.$$

Unfortunately, we can't compute when there are very many small particles $d \to 0$ at finite ϕ or $W \to \infty$ at finite ϕ. Our data shows that the observed wave length in the numerical simulation is decreasing function of d/W when the initial arrangement of particles is fixed (see Tables 1-6 and 8-11). The data suggests that there is a limiting value, depending on the initial arrangement, also for the two-fluid model as is indicated by the convergence of viscosity function exhibited in Figure VIII.9.

Figure VIII.9 shows a very strong effect of the walls; this arises as a consequence of the variation of d/W for a fixed d and by a perhaps serious mismatch of theory and numerical experiment which is amplified by reducing W. Nearby walls have a big effect when the no-slip condition at the side-walls is enforced, as in the numerical simulation. The no-slip condition is not enforced in the viscous potential flow theory; the retardation due to the walls is apparently realized in the model by a higher value of effective viscosity. This value is larger when the solids fraction is small because the shielding from the wall by other particles works less well when there are few than

when there are many particles. The viscous potential flow model, which apparently works well as a fully viscous two-fluid model for Rayleigh-Taylor instability, may not be good approximation when the walls are close. A fully viscous two-fluid model of Rayleigh-Taylor instability would probably give better results.

The initial lattice of particles is an important parameter in our effective property model of Rayleigh-Taylor instability. Rather large differences in the effective viscosity are demonstrated between square and rectangular lattices are exhibited in Figure VIII.11. Figures VIII.4(b) and VIII.4(c) exhibit an increase of local solid fraction near the interface. However, when we increased the diameter of the disks from 10/192 cm to 16/192 cm, this increase of local solid fraction is reduced dramatically (see Figure VIII.4(d)). An effective property model might be expected to work best in a statistically homogeneous media. The square and hexagonal arrangements are periodic in x and y with same period but the rectangular arrangement is doubly periodic.

The overall conclusion of this study is that effective two-fluid models can be made to work in particulate flow but such theories require a prior prescription of the domain of arrangements of particles to which the theory might apply. The greatest predictive value of such effective theories is for statistically homogeneous media.

Table VIII.1. The dimension of the box is $(W, L) = (4, 12)$ and H_2 varies from 5.6541 to 5.6831. The number of disks is $42 \times 60 = 2520$ (60 rows). The averaged particle Reynold number at the final time step varies from 2.226 to 1.692. Initial lattice is **square**.

Disk diameter	Solid fraction	Wave length and associated wave number K_0 (in cm^{-1})	Effective viscosity η_2 for which $n(K_0, \eta_2)$ is maximum	$n(K_0, \eta_2)$	Growth rate from simulation
10/192	23.74%	1.0, 2 0 π	0.14409	6.012	9.201
11/192	28.69%	0.8, 2.5 π	0.11135	7.380	10.237
12/192	34.10%	0.667, 3 0 π	0.09078	8.801	11.185
13/192	39.97%	0.615, 3.25π	0.08690	9.904	12.716
14/192	46.29%	0.571, 3.5 π	0.08346	11.044	14.645

Table VIII.2. The dimension of the box is $(W, L) = (6, 12)$ and H_2 varies from 5.6738 to 5.7031. The number of disks is $63 \times 60 = 3780$ (60 rows). The averaged particle Reynold number at the final time step varies from 2.248 to 1.296. Initial lattice is **square**.

Disk diameter	Solid fraction	Wave length and associated wave number K_0 (in cm^{-1})	Effective viscosity η_2 for which $n(K_0, \eta_2)$ is maximum	$n(K_0, \eta_2)$	Growth rate from simulation
10/192	23.66%	0.600, 3.33 π	0.06149	7.748	9.941
11/192	28.60%	0.545, 3.67 π	0.05821	8.924	10.451
12/192	34.01%	0.500, 4.00 π	0.05537	10.150	11.402
13/192	39.88%	0.4615. 4.33 π	0.05287	11.423	12.565
14/192	46.21%	0.4615, 4.33 π	0.05778	12.278	14.512
15/192	53.00%	0.429. 4.67 π	0.05506	13.623	14.536
16/192	60.25%	0.4138. 4.83 π	0.05593	14.756	13.917

Table VIII.3. The dimension of the box is $(W, L) = (8, 12)$ and H_2 varies from 5.6838 to 5.7059. The number of disks is $84 \times 60 = 5040$ (60 rows). The averaged particle Reynold number at the final time step varies from 2.261 to 1.278. Initial lattice is **square**.

Disk diameter	Solid fraction	Wave length and associated wave number K_0 (in cm^{-1})	Effective viscosity η_2 for which $n(K_0, \eta_2)$ is maximum	$n(K_0, \eta_2)$	Growth rate from simulation
10/192	23.61%	0.500, 4.00 π	0.04433	8.480	10.056
11/192	28.56%	0.471, 4.25 π	0.04462	9.600	10.712
12/192	33.96%	0.444, 4.50 π	0.04474	10.758	11.377
13/192	39.83%	0.432, 4.625 π	0.04698	11.795	12.503
14/192	46.17%	0.421, 4.75 π	0.04903	12.849	14.377
15/192	52.96%	0.41025, 4.875 π	0.05091	13.919	13.849
16/192	60.22%	0.41025, 4.875 π	0.05507	14.816	15.039

Table VIII.4. The dimension of the box is $(W, L) = (10, 12)$ and H_2 varies from 5.6899 to 5.7075. The number of disks is $105 \times 60 = 6300$ (60 rows). The averaged particle Reynold number at the final time step varies from 2.268 to 1.276. Initial lattice is **square**.

Disk diameter	Solid fraction	Wave length and associated wave number K_0 (in cm^{-1})	Effective viscosity η_2 for which $n(K_0, \eta_2)$ is maximum	$n(K_0, \eta_2)$	Growth rate from simulation
10/192	23.59%	0.455, 4.4 π	0.03707	8.889	9.979
11/192	28.53%	0.435, 4.6 π	0.03848	9.983	10.544
12/192	33.93%	0.4167, 4.8 π	0.03967	11.107	11.313
13/192	39.81%	0.4167, 4.8 π	0.04388	12.012	12.283
14/192	46.14%	0.4000, 5.0 π	0.04464	13.179	13.795
15/192	52.94%	0.39215, 5.1 π	0.04691	14.233	14.366
16/192	60.20%	0.37736, 5.3 π	0.04739	15.446	14.081

Table VIII.5. The dimension of the box is $(W, L) = (12, 12)$ and H_2 varies from 5.6939 to 5.7087. The number of disks is $126 \times 60 = 7560$ (60 rows). The averaged particle Reynold number at the final time step varies from 2.272 to 1.695. Initial lattice is **square**.

Disk diameter	Solid fraction	Wave length and associated wave number K_0 (in cm^{-1})	Effective viscosity η_2 for which $n(K_0, \eta_2)$ is maximum	$n(K_0, \eta_2)$	Growth rate from simulation
10/192	23.57%	0.429, 4.667 π	0.03308	9.151	10.022
11/192	28.51%	0.414, 4.833 π	0.03500	10.230	10.570
12/192	33.92%	0.400, 5.000 π	0.03671	11.333	11.308
13/192	39.79%	0.400, 5.000 π	0.04066	12.257	12.308
14/192	46.12%	0.387, 5.167 π	0.04201	13.394	14.250

Table VIII.6. The dimension of the box is $(W, L) = (10, 12)$ and H_2 varies from 7.5865 to 7.6101. The number of disks is $105 \times 80 = 8400$ (80 rows). The averaged particle Reynold number at the final time step varies from 2.268 to 1.264. Initial lattice is **square**.

Disk diameter	Solid fraction	Wave length and associated wave number K_0 (in cm^{-1})	Effective viscosity η_2 for which $n(K_0, \eta_2)$ is maximum	$n(K_0, \eta_2)$	Growth rate from simulation
10/192	23.59%	0.47629, 4.2 π	0.04047	8.685	9.788
11/192	28.53%	0.45454, 4.4 π	0.04183	9.763	10.435
12/192	33.93%	0.43478, 4.6 π	0.04295	10.873	11.255
13/192	39.81%	0.41667, 4.8 π	0.04388	12.012	12.259
14/192	46.14%	0.40816, 5.0 π	0.04464	13.179	13.527
15/192	52.94%	0.38462, 5.2 π	0.04528	14.372	14.080
16/192	60.20%	0.37037, 5.4 π	0.04580	15.591	13.857

Table VIII.7. The dimension of the box is $(W, L) = (10, 12)$ and H_2 varies from 5.6899 to 5.7017. The number of disks is $105 \times 60 = 6270$. The averaged particle Reynold number at the final time step varies from 2.259 to 2.089. Initial lattice is **hexagonal**.

Disk diameter	Solid fraction	Wave length and associated wave number K_0 (in cm^{-1})	Effective viscosity η_2 for which $n(K_0, \eta_2)$ is maximum	$n(K_0, \eta_2)$	Growth rate from simulation
10/192	23.48%	0.476, 4.20 π	0.04035	8.664	8.870
11/192	28.39%	0.455, 4.40 π	0.04170	9.740	9.257
12/192	33.77%	0.434, 4.60 π	0.04282	10.848	9.722
13/192	39.62%	0.417, 4.80 π	0.04374	11.984	10.513
14/192	45.92%	0.400, 5.00 π	0.04451	13.148	12.226

Table VIII.8. The dimension of the box is $(W, L) = (8, 12)$ and H_2 varies from 5.3711 to 5.7812. The number of disks is $80 \times 60 = 4800$ (60 rows). The averaged particle Reynold number at the final time step varies from 2.591 to 1.552. Initial lattice is **rectangular**.

Disk diameter	Solid fraction	Wave length and associated wave number K_0 (in cm^{-1})	Effective viscosity η_2 for which $n(K_0, \eta_2)$ is maximum	$n(K_0, \eta_2)$	Growth rate from simulation
10/192	23.80%	1.14286, 1.75 π	0.17849	5.630	8.632
11/192	28.44%	1.0, 2.0 π	0.15883	6.572	9.723
12/192	33.42%	0.8889, 2.25 π	0.14358	7.548	10.679
13/192	38.74%	0.8421, 2.375 π	0.14268	8.338	13.034
14/192	44.39%	0.7619, 2.625 π	0.13084	9.370	13.508
15/192	50.35%	0.6956, 2.875 π	0.12105	10.428	15.038
16/192	56.61%	0.64, 3.125 π	0.11281	11.511	14.518

Table VIII.9. The dimension of the box is $(W, L) = (8, 12)$ and H_2 varies from 7.1614 to 7.7083. The number of disks is $80 \times 80 = 6400$ (80 rows). The averaged particle Reynold number at the final time step varies from 2.593 to 1.523. Initial lattice is **rectangular**.

Disk diameter	Solid fraction	Wave length and associated wave number K_0 (in cm^{-1})	Effective viscosity η_2 for which $n(K_0, \eta_2)$ is maximum	$n(K_0, \eta_2)$	Growth rate from simulation
10/192	23.80%	1.14286, 1.75 π	0.17850	5.630	8.298
11/192	28.44%	1.0, 2.0 π	0.15883	6.572	9.591
12/192	33.42%	0.8889, 2.25 π	0.14358	7.548	10.553
13/192	38.74%	0.8421, 2.375 π	0.14268	8.338	12.785
14/192	44.39%	0.7619, 2.625 π	0.13084	9.370	13.136
15/192	50.35%	0.6956, 2.875 π	0.12105	10.428	14.253
16/192	56.61%	0.64, 3.125 π	0.11281	11.511	13.900

Table VIII.10. The dimension of the box is $(W, L) = (10, 12)$ and H_2 is 7.7109. The number of disks is $100 \times 80 = 8000$ (80 rows). The averaged particle Reynold number at the final time step is 0.857. Initial lattice is **rectangular**.

Disk diameter	Solid fraction	Wave length and associated wave number K_0 (in cm^{-1})	Effective viscosity η_2 for which $n(K_0, \eta_2)$ is maximum	$n(K_0, \eta_2)$	Growth rate from simulation
16/192	56.59%	0.6061, 3.3 π	0.10315	11.827	13.959

Table VIII.11. The dimension of the box is $(W, L) = (8, 12)$ and H_2 varies from 5.6988 to 5.7047. The numbers of disks are $116 \times 83 = 9628$ (83 rows) and $126 \times 90 = 11340$ (90 rows). The averaged particle Reynold number at the final time step varies from 1.031 to 1.536. Initial lattice is **square**.

Disk diameter	Solid fraction	Wave length and associated wave number K_0 (in cm^{-1})	Effective viscosity η_2 for which $n(K_0, \eta_2)$ is maximum	$n(K_0, \eta_2)$	Growth rate from simulation
8/192	28.77%	0.3478, 5.75 π	0.02484	11.207	11.914
8/192	33.92%	0.4, 5 π	0.03671	11.333	12.736

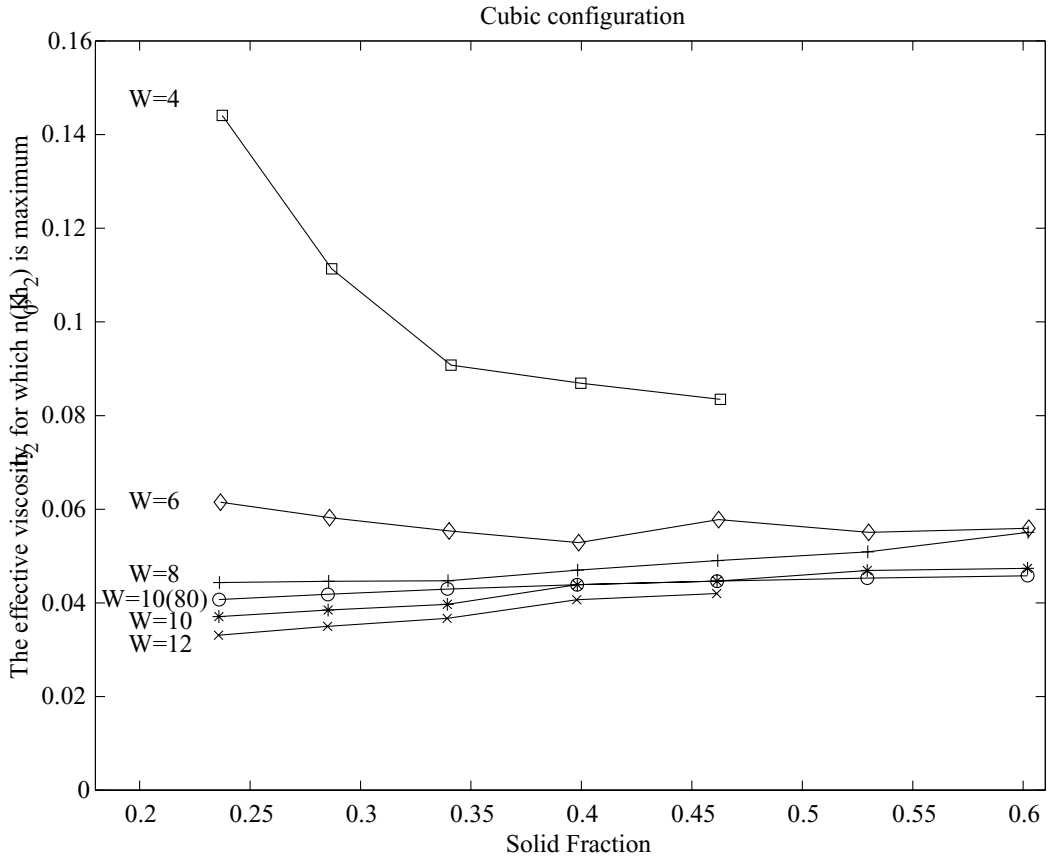

Figure VIII.9: *The effective viscosity η_2 for which $n(K_0, \eta_2)$ is maximum: the width of box is W varying from 4 cm to 12 cm, and height of box is 12 cm, the initial lattice is square, the number of rows is 60 (except the case $W = 10(80)$ in which there are 80 rows), the number of column varies from 42 to 126, and the diameter of disks varies from 10/192 cm to 16/192 cm.*

Table VIII.12. The dimension of the box is $(W, L) = (8, 12)$ and H_2 is 5.6838. The number of disks is 5040. The averaged particle Reynold number at the final time step is 3.022. Initial lattice is **disordered**.

Disk diameter	Solid fraction	Wave length* and associated wave number K_0 (in cm^{-1})	Effective viscosity η_2 for which $n(K_0, \eta_2)$ is maximum	$n(K_0, \eta_2)$	Growth rate from simulation
10/192	23.61%	0.4444, 4.5 π	0.03553	8.994	9.730

* The wave length is an averaged quantity in this case due to the irregular shape of waves.

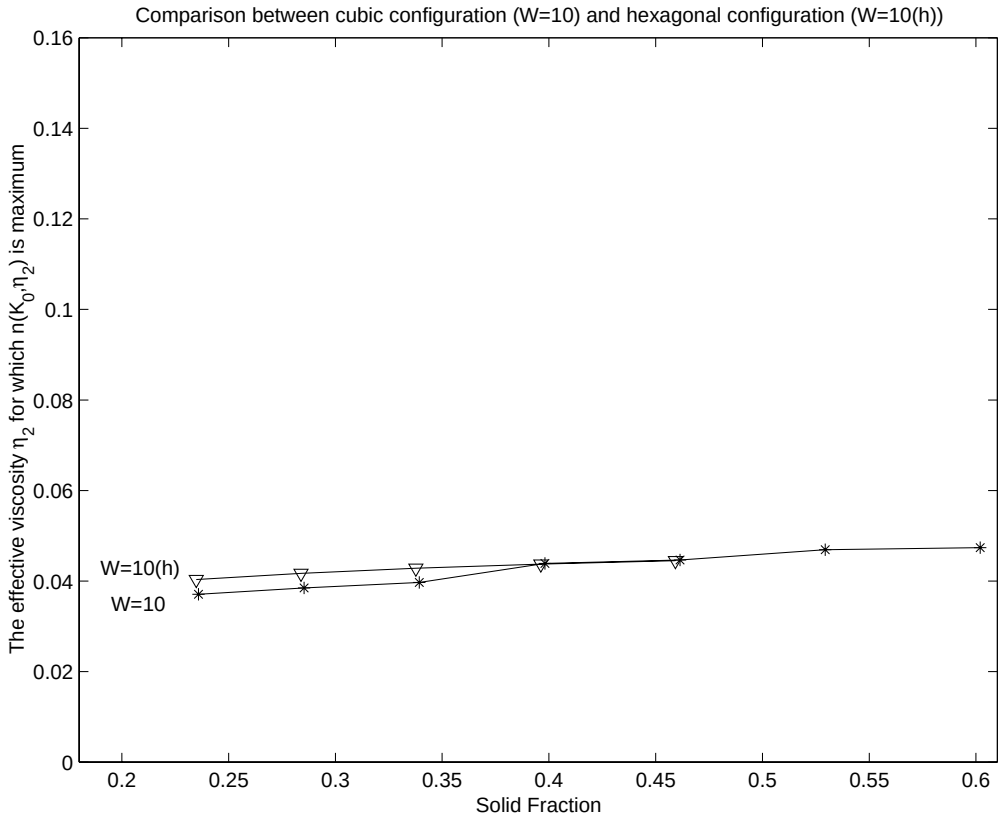

Figure VIII.10: *The comparison of the effective viscosity η_2 (for which $n(K_0, \eta_2)$ is maximum): the width of box is $W = 10$ cm, the height of box is 12 cm, the initial lattice is either square ($W = 10$) and hexagonal ($W = 10(h)$), the number of rows is 60, the number of column is 105, and the diameter of disks varies from 10/192 cm to 16/192 cm.*

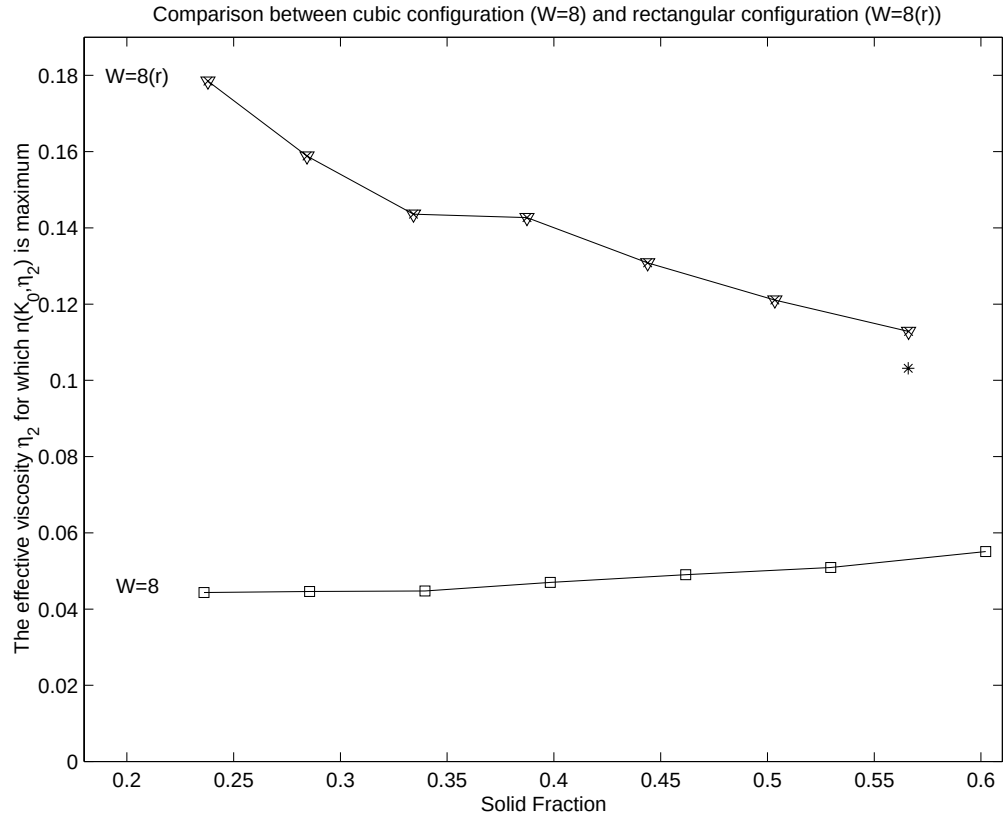

Figure VIII.11: *The comparison of the effective viscosity η_2 (for which $n(K_0, \eta_2)$ is maximum): the width of box is $W = 8$ cm, the height of box is 12 cm, the initial lattice is either square ($W = 8$) and rectangular ($W = 8(r)$), the number of rows in square case is 60, those of rectangular case are 60 and 80, the number of column is 80, the diameter of disks varies from 10/192 cm to 16/192 cm. Cases in which there 60 rows (resp., 80 rows) and 80 columns of disks are marked by ∇ (resp., "x"). The "*" is a case in which there 100 rows and 80 columns of disks of diameter 16/192 cm.*